This is an open access article published under a Creative Commons Non-Commercial No Derivative Works (CC-BY-NC-ND) Attribution License, which permits copying and redistribution of the article, and creation of adaptations, all for non-commercial purposes.

Article

Cite This: J. Phys. Chem. C 2018, 122, 17612−17620

pubs.acs.org/JPCC

New Route for "Cold-Passivation" of Defects in Tin-Based Oxides

Esteban Rucavado,*[,†] Miglė Graužinytė,[‡] José A. Flores-Livas,[‡] Quentin Jeangros,[†,‡] Federica Landucci,[†,§] Yeonbae Lee,[∥] Takashi Koida,[⊥] Stefan Goedecker,[‡] Aïcha Hessler-Wyser,[†] Christophe Ballif,[†] and Monica Morales-Masis*[,†,#]

[†]Institute of Microengineering (IMT), Photovoltaics and Thin-Film Electronics Laboratory, École Polytechnique Fédérale de Lausanne (EPFL), Neuchâtel CH-2002, Switzerland

[‡]Department of Physics, Universität Basel, Klingelbergstr. 82, 4056 Basel, Switzerland

[§]Interdisciplinary Centre for Electron Microscopy, École Polytechnique Fédérale de Lausanne (EPFL), Lausanne CH-1015, Switzerland

[∥]Department of Materials Science and Engineering, University of California Berkeley, Berkeley, California 94720, United States

[⊥]Research Center for Photovoltaics, National Institute of Advanced Industrial Science and Technology (AIST), Tsukuba, Ibaraki 305-8568, Japan

[#]MESA+ Institute for Nanotechnology, University of Twente, 7500 AE Enschede, The Netherlands

Supporting Information

ABSTRACT: Transparent conductive oxides (TCOs) are essential in technologies coupling light and electricity. For Sn-based TCOs, oxygen deficiencies and undercoordinated Sn atoms result in an extended density of states below the conduction band edge. Although shallow states provide free carriers necessary for electrical conductivity, deeper states inside the band gap are detrimental to transparency. In zinc tin oxide (ZTO), the overall optoelectronic properties can be improved by defect passivation via annealing at high temperatures. Yet, the high thermal budget associated with such treatment is incompatible with many applications. Here, we demonstrate an alternative, low-temperature passivation method, which relies on cosputtering Sn-based TCOs with silicon dioxide (SiO_2). Using amorphous ZTO and amorphous/polycrystalline tin dioxide (SnO_2) as representative cases, we demonstrate through optoelectronic characterization and density functional theory simulations that the SiO_2 contribution is twofold. First, oxygen from SiO_2 passivates the oxygen deficiencies that form deep defects in SnO_2 and ZTO. Second, the ionization energy of the remaining deep defect centers is lowered by the presence of silicon atoms. Remarkably, we find that these ionized states do not contribute to sub-gap absorptance. This simple passivation scheme significantly improves the optical properties without affecting the electrical conductivity, hence overcoming the known transparency−conductivity trade-off in Sn-based TCOs.

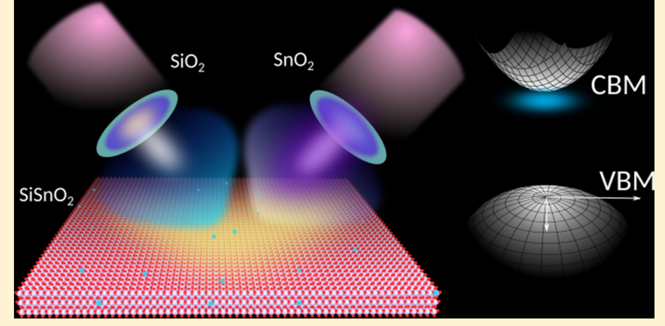

INTRODUCTION

Sn-based oxides are wide band gap semiconductors of high technological importance, with applications ranging from smart windows to batteries and solar cells. The optoelectronic properties of tin dioxide (SnO_2) can be tuned over a wide range of conductivity and transparency and, hence, adapted to the requirements of each of these technologies. For example, reported electrical conductivity values span from[1] $\sim 10^{-6}$ to[2] 10^4 S cm^{-1}. This is achieved by tuning the density of oxygen deficiencies (V_O) or by adding dopants such as fluorine, antimony, barium, or molybdenum.[3−7] Other elements may be added to transparent conductive oxides (TCOs) to modify, for example, their microstructure and thermal stability.[8] In this regard, the addition of zinc to SnO_2 [zinc tin oxide (ZTO)] yields thin films with attractive properties such as a total transmittance higher than 75% in the visible and near-infrared spectral range[9−11] and an amorphous microstructure when deposited at room temperature, which is preferable for applications in flexible and organic devices.[12] Furthermore, this microstructure remains stable up to temperatures as high as 550 °C.[11,13] Because of these properties, ZTO has already been applied as a transparent contact in organic light-emitting diodes,[12,14] as a channel in thin film transistors,[15,16] and as a recombination layer in silicon-perovskite tandem solar cells.[17] Theoretical and experimental evidence suggests that the presence of oxygen deficiencies in ZTO creates both shallow and deep sub-gap states, with the latter acting as absorption centers in the visible part of the spectrum.[11,18,19] Even though

Received: March 8, 2018
Revised: July 17, 2018
Published: July 17, 2018

Downloaded via ECOLE POLYTECHNIC FED LAUSANNE on January 26, 2021 at 15:31:00 (UTC).
See https://pubs.acs.org/sharingguidelines for options on how to legitimately share published articles.

© 2018 American Chemical Society

these defects can be passivated by postdeposition treatments in air at temperatures >400 °C,[11] annealing in these conditions is thermally costly and/or not convenient for devices with low thermal budgets, such as solar cells based on thin hydrogenated amorphous silicon layers or hybrid organic−inorganic perovskite materials.[20−22]

Alternatively, previous investigations have shown that the codeposition of silicon dioxide (SiO_2) with different TCOs, mainly with zinc oxide, may decrease the density of V_O defects[23−26] but also lower the refractive index,[23,27] decrease the resistivity,[27−29] and amorphize the TCO.[28,30,31] For the case of Si in Sn-based TCOs, Kang and co-workers[26] used first-principle calculations to suggest that silicon atoms alter the coordination number of Sn, leading to an increase in the formation energy of V_O deficiencies. Yet, this passivation mechanism leads to a strong decrease in electrical conductivity as these deficiencies are the source of free carriers. Furthermore, it was recently proposed that Si modifies the band gap of ZTO, resulting in improved TFT performance.[32] However, the role of Si in the sub-gap structure of ZTO was not fully clarified at the atomistic level in this study. In contrast to previous reports, here we combine experimental and computational techniques to explain the effect of Si on the optoelectronic properties of SnO_2-based materials. We demonstrate that adding SiO_2 during deposition of Sn-based TCOs (using ZTO and SnO_2, as case examples) results in a decrease in the sub-gap absorption while keeping electrical properties unchanged. By combining these experimental results with density functional theory (DFT) calculations, we find that, while the oxygen from SiO_2 passivates deep sub-gap defects, the addition of Si decreases the ionization energy of V_O and shifts the corresponding sub-gap defect states close to the conduction band minimum (CBM). Thanks to this effect, the defect no longer contributes to the formation of detrimental sub-gap absorption centers and provides free carriers.

RESULTS

Trade-Off in Optoelectronic Properties of ZTO. Before optimizing ZTO by cosputtering with SiO_2, the properties of ZTO films were studied as a function of O_2 flow during deposition. As seen in Figure 1, ZTO films sputtered with a low O_2 flow during deposition (1.5−2.5 sccm of Ar−O_2) present low conductivity and high absorption in the measured spectral range. Initially, increasing the O_2 content improves the film transparency, and its conductivity reaches a maximum of 456 S cm^{-1}. Increasing the Ar−O_2 flow above 3.0 sccm reduces the optical absorptance but at the expense of conductivity, which drops by 62%. A trade-off often observed in TCOs is reached: improving the optical properties worsens the electrical ones and vice-versa. As observed in Figure 1, optimizing the oxygen flow during deposition does not yield a film that combines a conductivity above 400 S cm^{-1} and a low absorptance at 500 nm (≤5%). Alternative approaches are, hence, required to control the amount of oxygen in the films and to ensure both high conductivity and transparency.

Combinatorial Deposition of SiO_2 and Sn-Based TCOs. To introduce oxygen into Sn-based TCOs in a precise manner, while avoiding high temperature steps,[11] ZTO or SnO_2 was cosputtered with SiO_2. In the following subsections, we describe in detail the optimization and characterization of ZTO with SiO_2 (referred to as SiZTO). The ZTO film with highest conductivity (3.0 sccm of Ar−O_2, a composition reported in refs 11 and 14) will be used as a reference to assess the effectiveness of cosputtering deposition with SiO_2. Experimental details of the optimization of SnO_2 with SiO_2 ($SiSnO_2$) are described in Section I of the Supporting Information.

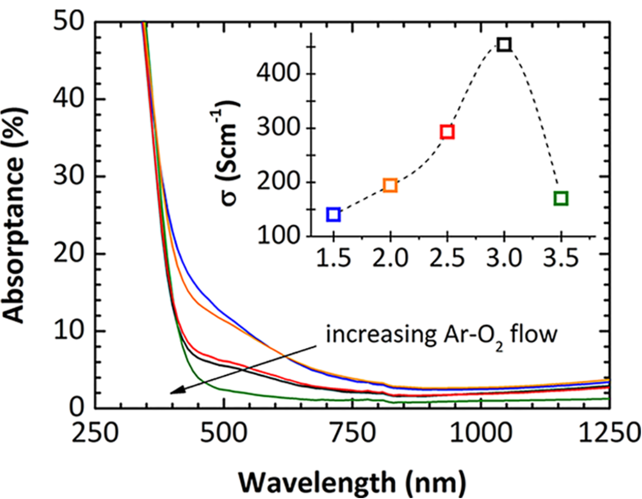

Figure 1. Absorptance of ZTO films as a function of the oxygen flow during deposition. The inset shows the change in conductivity for the same samples. All films were annealed at 200 °C for 30 min in air prior to the measurements.

Reducing Sub-gap Absorption in ZTO Thin Films. We determined the optimal deposition conditions (regarding SiO_2 content and Ar−O_2 flow), by comparing a simplified figure of merit (FOM) of films sputtered under different conditions. The FOM was calculated as follows: $\mathrm{FOM} = \frac{\sigma}{A_{400-800}}$, where σ is the electrical conductivity and $A_{400-800}$ is the average absorptance from 400 to 800 nm. Therefore, a high FOM is indicative of films with high electrical conductivity and/or low absorptance in the visible spectral range. The SiZTO films with the highest FOM were deposited using 10 W (0.13 W cm^{-2}) in the SiO_2 target and 2.5 sccm of Ar−O_2 (marked with dashed lines in Figure 2a). More information about the deposition details can be found in the Methods section. The evolution of the electrical properties of SiZTO with SiO_2 content is shown in Figure 2b (all films deposited with an Ar−O_2 flow of 2.5 sccm). The electron mobility increases from 22.2 cm^2 V^{-1} s^{-1} up to a maximum of 26.8 cm^2 V^{-1} s^{-1} when the power applied to the SiO_2 target is increased from 0 to 10 W. For these powers, the free carrier density remains constant at 1×10^{20} cm^{-3}. Further, increasing the SiO_2 content makes the films less absorbing, but it also results in a decrease of free carrier density and mobility.

To highlight the effect of adding SiO_2 to ZTO, the conductivity and absorptance of the optimized SiZTO and the ZTO reference are compared in Figure 3. It is worth noting that only a slight difference in conductivity between ZTO and SiZTO is observed (208 and 192 S cm^{-1} for as-deposited films and 454 vs 429 S cm^{-1} after a mild annealing at 200 °C), with the clear advantage of SiZTO presenting less absorptance than ZTO in this wavelength range. Indeed, at a wavelength of 500 nm, ZTO has a 5.5% absorptance, whereas SiZTO has an absorptance of only 2.5%. At wavelengths above 1000 nm, SiZTO exhibits an absorptance below 5% (Figure SI2).

SiZTO Microstructure and Composition. Nanobeam diffraction patterns of the optimized SiZTO films (10 W in

DOI: 10.1021/acs.jpcc.8b02302
J. Phys. Chem. C 2018, 122, 17612−17620

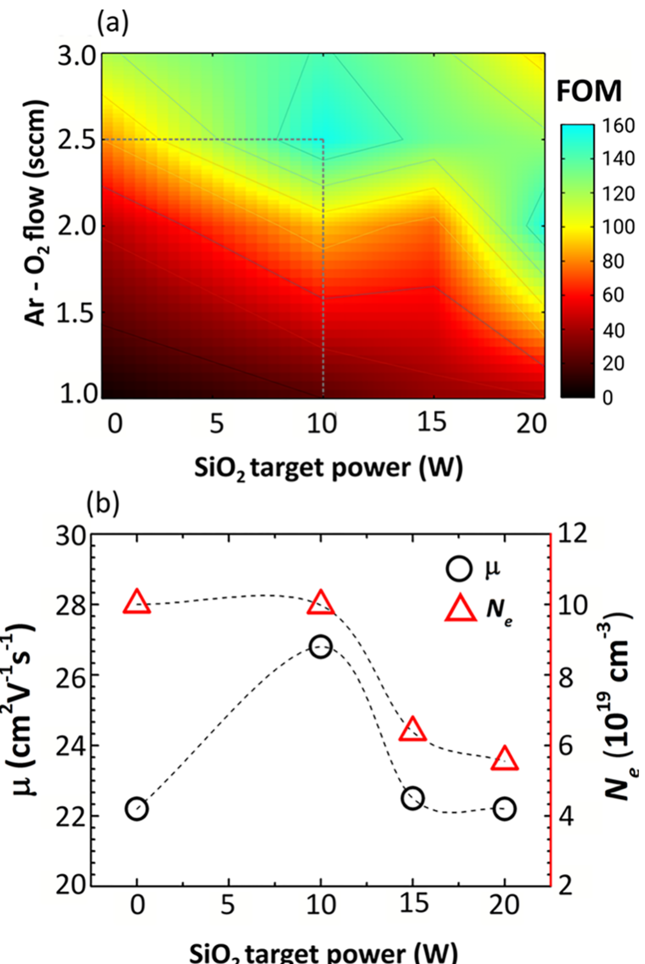

Figure 2. (a) Plot of the FOM as a function of deposition parameters. The FOM was calculated as the ratio of conductivity and average absorptance in the range of 400−800 nm for SiZTO films deposited with different SiO_2 and O_2 content; (b) Hall mobility and free carrier density of SiZTO as a function of power applied on the SiO_2 target; these films had a constant $Ar-O_2$ flow of 2.5 sccm.

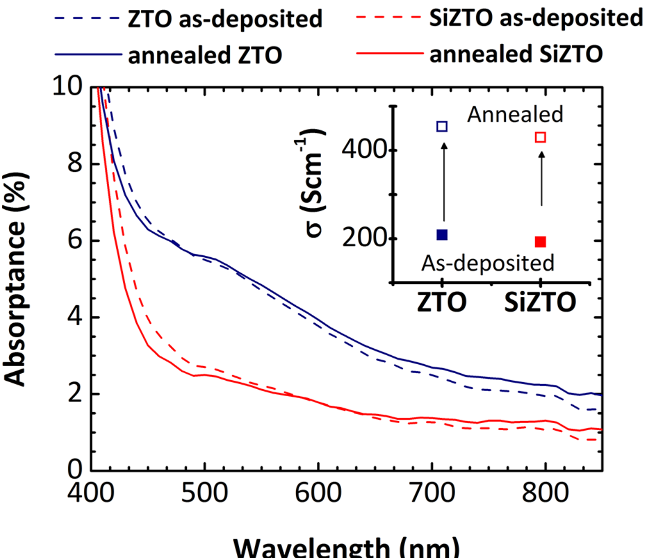

Figure 3. Absorptance and conductivity (inset) of optimized SiZTO (10 W in the SiO_2 target and 2.5 sccm of $Ar-O_2$) and ZTO as-deposited and after annealing at 200 °C. Although both films show virtually equal conductivities, SiZTO presents a lower absorptance below the band gap when compared to the reference ZTO.

the SiO_2 target and 2.5 sccm of $Ar-O_2$) indicate an amorphous microstructure (Figure 4a), analogous to that of ZTO.[11] A scanning transmission electron microscopy (STEM) high-angle annular dark-field (HAADF) image and an energy-dispersive X-ray spectroscopy (EDX) analysis of the cross-section of the optimized SiZTO film (deposited on sapphire) are shown in Figure 4b,c. The HAADF image of the cross section of the sample indicates a dense and homogeneous microstructure (Figure 4c), whereas the EDX line profiles demonstrate that the distribution of elements is uniform within the amorphous film. A slight Si accumulation is measured at the top of the film because the SiO_2 target shutter was closed slightly after one of the ZTO.

The composition of the optimized SiZTO film determined by Rutherford backscattering (RBS) is $Si_{0.02}Zn_{0.04}Sn_{0.27}O_{0.67}$, indicating an absolute increase in oxygen concentration of 2 at. % when compared to the reference ZTO ($Zn_{0.05}Sn_{0.30}O_{0.65}$). EDX and RBS yield a similar composition. In addition, thermal desorption spectroscopy demonstrates that, when heating the films up to 700 °C, the total oxygen desorption of SiZTO is higher than that for ZTO (area under the curve in Figure SI4 of the Supporting Information). Furthermore, the onset of effusion of Zn is postponed to higher temperatures when Si atoms are present in the film. These results suggest that the film decomposition may be postponed to higher temperatures with the addition of Si. Similar to the presence of Zn within the amorphous SnO_2, the smaller Si atoms could induce local strain in the amorphous network postponing decomposition.[13]

X-ray photoelectron spectroscopy (XPS) was performed on the optimized ZTO and SiZTO films (before and after annealing) to evaluate the possible changes in the oxidation state of the elements present when adding SiO_2 and/or after annealing, which could explain the observed changes in optoelectronic properties. For O 1s, Sn 3d, and Zn 2p bands, a pseudo-Voigt function was fitted to the data to calculate the binding energies and the full width at half maximum. No important differences in the fitted values are seen between the measured samples (Supporting Information Figure SI5). In addition, no signal above the background was observed for the Si 2p peak at the corresponding binding energies, which indicates that the Si content is below the detection limit in these experiments.[33,34]

Addition of SiO_2 to SnO_2: General Procedure for Sn-Based TCOs. To test the universality of adding SiO_2 to improve the optoelectronic properties of Sn-based TCOs, SiO_2 was cosputtered this time with pure SnO_2. Details about the combinatorial sputtering of $SiSnO_2$ and microstructure of SnO_2 are described in Section I of the Supporting Information. A detailed overview of the microstructure of $SiSnO_2$, described by transmission electron microscopy (TEM), is shown in Figure 4d−f. The section of the $SiSnO_2$ film in contact with the substrate is amorphous, however, as the material thickens, it crystallizes into rutile c-SnO_2 structure. Nanocrystallites are formed halfway through the 150 nm thick film. A composition of $Sn_{0.38}O_{0.62}$ is obtained by EDX before SiO_2 addition. For SiZTO, EDX indicates that Si is homogenously distributed at an average value of 3 at. % within the films, whereas the oxygen content increases slightly to 63 at. %. Furthermore, Si atoms do not accumulate at grain boundaries or inside the bulk (amorphous or crystalline) of $SiSnO_2$ (see Si map in Figure

DOI: 10.1021/acs.jpcc.8b02302
J. Phys. Chem. C 2018, 122, 17612−17620

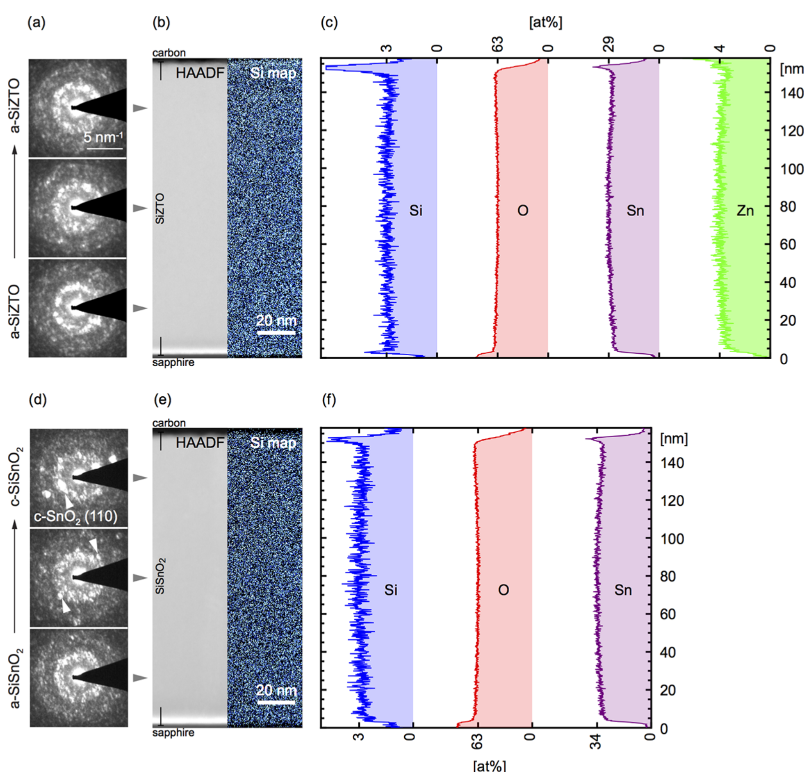

Figure 4. (a) Nanobeam electron diffraction patterns taken along the growth direction of SiZTO thin films. The asymmetric speckles indicate an amorphous structure, unchanged with SiO_2 addition[11] and along the growth axis; (b) STEM HAADF image of the cross section of the film (left panel) corresponding to Si K edge EDX map (right panel); (c) at. % line profiles (left to right) of the Si K, O K, Sn L, and Zn K edges quantified using the FEI Velox software (assuming a sample thickness of 100 nm and a density of 6.5 g/cm^3 for the absorption correction); (d) nanobeam electron diffraction taken along the growth direction of $SiSnO_2$, showing an increased crystallinity toward the end of the film (arrowheads); (e) STEM HAADF image of the cross section of the film and Si EDX map; (f) quantified line profiles of the elements of interest.

4e). No Si-rich clusters are observed, particularly toward the top of the film, where the film is composed of small crystallites (Figure 4d). As seen in Figure 5, the conductivity of the as-deposited and annealed SnO_2 drops slightly when adding 3 at. % of Si, whereas the absorptance in the visible and near-infrared regions decreases simultaneously (from 6 to 3% at 500 nm). Hall effect measurements indicate a free carrier density of 1.75×10^{20} cm^{-3} for SnO_2 and 1.26×10^{20} cm^{-3} for $SiSnO_2$, and mobilities of 28.2 and 25.5 cm^2 V^{-1} s^{-1} for SnO_2 and $SiSnO_2$, respectively. Notably, the SnO_2 film contains both amorphous and polycrystalline regions (Supporting Information Section I) demonstrating that the addition of SiO_2 passivates the sub-gap defects in amorphous and mixed-phase amorphous/polycrystalline thin films. In addition, the presence of Si-atoms in SnO_2 retards the onset of crystallization of the films: grains start to appear closer to the top surface in $SiSnO_2$ when compared to SnO_2. A similar effect has been previously reported for Zn-modification of SnO_2.[13] Finally, the presence/lack of Zn does not appear to modify the passivation mechanism.

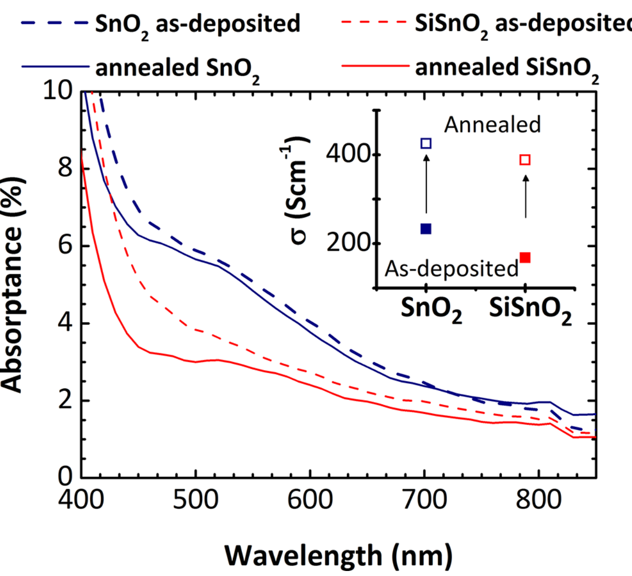

Figure 5. Absorptance and conductivity (inset) of as-deposited and annealed SiO_2–SnO_2 ($SiSnO_2$) and SnO_2 films. The films were deposited at the optimal conditions. As for ZTO, both films show similar conductivities. The main advantage of $SiSnO_2$ films is their lower absorption in the visible range.

Computational Assessment of Si Modification to SnO_2. The addition of a small amount of SiO_2 does not modify the microstructure of ZTO, which remains amorphous, yet improves the optical properties of the film. The gain in optical properties occurs irrespective of whether the microstructure is fully amorphous (SiZTO) or an amorphous/polycrystalline mixture ($SiSnO_2$). Moreover, both Si and O are found by EDX to be homogeneously distributed within the thin films and show no segregation (e.g., Si does not accumulate at the grain boundaries of the polycrystalline SnO_2 structure, as shown in Figure 4d–f). These observations indicate that the addition of SiO_2 is modifying the nature of point defects present within the films; point defects must be present in both amorphous

DOI: 10.1021/acs.jpcc.8b02302
J. Phys. Chem. C 2018, 122, 17612−17620

and crystalline structures. To understand in detail the nature of these defects and their passivation mechanism by Si addition, DFT calculations were performed. For these calculations, the rutile crystal structure of SnO_2 was used as a starting point because (i) the same effect was observed for amorphous and polycrystalline structures, (ii) ZTO crystallizes into rutile SnO_2 and has first coordination shells very close to this atomic structure,[13] (iii) Zn does not appear to modify the Si-passivation mechanism (see previous paragraph), and (iv) in a crystalline structure, the effects induced by point defects can be isolated and only a limited number of defect sites needs to be considered compared to an amorphous environment, thus preventing the convolution of different effects (i.e., induced by the aperiodic structure and/or locally missing atoms) that may blur the contribution of individual point defects in an amorphous material.

The stoichiometric phase of crystalline SnO_2 has a defect-free band gap of 3.6 eV with no parasitic absorption in the visible range.[35] One possible cause for the optical absorption feature shown in Figure 5 is deep-defect states arising from charge-neutral oxygen vacancies predicted by theoretical models.[18,19] A similar role of oxygen-deficiency-related defects in the sub-gap absorptance was demonstrated for the amorphous ZTO films in ref 11. The link between V_O-related defects and the absorptance features at 600 nm observed in Figure 3 is further supported by the observation that increasing oxygen partial pressure during deposition suppresses the absorption (Figure 1). The central role of oxygen deficiencies in the sub-gap absorption and its reduction in the presence of silicon suggest an indirect or direct passivation mechanism of the vacancies upon SiO_2 addition. In this section, one such possible mechanism is discussed by considering a direct interaction between Si and oxygen vacancies. First, the contribution of oxygen vacancies to the parasitic absorption in SnO_2 is described in detail and then the impact of Si addition is elucidated.

Oxygen Vacancies. The structure of the SnO_2 crystal containing an oxygen vacancy is shown in Figure 6a. Local relaxations of the three-neighboring tin atoms following the creation of an oxygen vacancy result in two symmetry inequivalent Sn-sites labeled site (A) and site (B) in the inset of Figure 6a. An isolated V_O is seen to be stable in two charge states in the crystalline SnO_2 film (see Figure 6b): an ionized $q = +2$ charge state when the Fermi level is below 2.77 eV and in a charge neutral $q = 0$ state when the Fermi level is approaching the conduction band. In agreement with the previous studies,[36−38] we observe electronic defect states in the mid-gap region for a charge neutral V_O (Figure 7a), which would contribute to parasitic absorption. In contrast, a doubly ionized V_O (Figure 7b) results in electronic states at the edge of the CBM of stoichiometric SnO_2, which would not detrimentally affect the optical properties of TCO. This transition of electronic defect states from deep to shallow is a result of local atomic relaxations that follow the ionization of the vacancy. Similar metastable shallow donor state formation via ionization has also been reported for other TCOs, namely ZnO and In_2O_3.[39,40]

Whether an oxygen vacancy contributes to parasitic absorption or not is, therefore, determined by the position of the Fermi level, ϵ_F. The Fermi energy at which two different charge states of a given defect have the same formation energy (i.e., form in equal concentrations according to Boltzmann statistics) is known as the thermodynamic transition level. The calculated thermodynamic transition levels, $\epsilon(2/0)$, are indicated by gray lines in Figure 6. In the case of an isolated oxygen vacancy, the $\epsilon(2/0)$ transition was found to occur at a Fermi level of 2.77 eV above the valence band. However, in an n-type TCO material, ϵ_F is expected to lie at or above the CBM. The distance, Δ, between the CBM and the thermodynamic transition level is, therefore, the quantity that determines the ratio between the concentrations, C_q, in which the different charge states, q, will form.

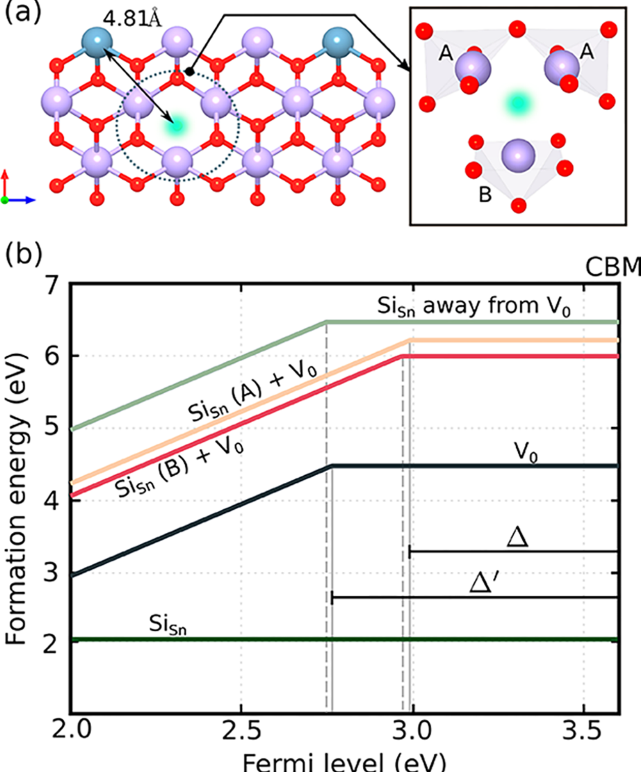

Figure 6. (a) SnO_2 surrounding an oxygen vacancy defect. Sn atoms are shown as purple spheres, oxygen—red, Si—blue, and the vacancy is indicated in green. Right panel: A and B number the two substitutional Si sites neighboring the vacancy. Left panel: The distance between a substitutional Si_{Sn} far from V_O is indicated; (b) formation energies (O-rich) of isolated defects and defect-clusters as a function of the Fermi level. $\epsilon(2/0)$ transitions are indicated by light gray lines. Δ marks the distance between $\epsilon(2/0)$ transition and the CBM. This distance, important in determining the ratio between different charge states, is shifted toward the CBM in the presence of Si.

$$\frac{C_0}{C_2} = \exp\left(\frac{2\Delta}{k_B T}\right) \quad (1)$$

In the case of an isolated V_O, a value of 0.855 eV for Δ was obtained. As a consequence, in an n-type SnO_2, the majority of oxygen vacancies is expected to be charge-neutral and likely to lead to parasitic absorption.

Addition of Silicon. The EDX measurements reveal a uniform distribution of Si atoms in the SnO_2 and ZTO atomic networks; hence, Si clustering in the modeling process was not considered. The rutile structure of SnO_2 offers two obvious substitutional sites for Si incorporation: the oxygen, Si_O, or the tin, Si_{Sn}, site. We found that silicon preferentially substitutes Sn with a formation energy of 2.04 eV and remains electrically inactive for Fermi levels across the band gap, as demonstrated

DOI: 10.1021/acs.jpcc.8b02302
J. Phys. Chem. C 2018, 122, 17612−17620

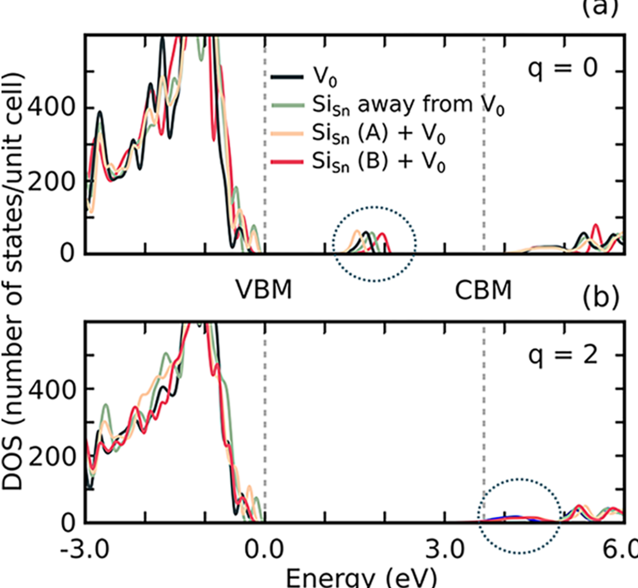

Figure 7. Electronic densities of states for oxygen-vacancy-related defects in SnO_2. Results for the charge neutral ($q = 0$) and for doubly ionized ($q = 2$) supercells are shown. Colored lines correspond to defect geometries described in detail in the main text. Defect-induced states are highlighted by dashed circles. (Left) Cold-passivation of Sn-based TCOs by cosputtering with SiO_2: a new method to design materials with enhanced optoelectronic properties. (Right) General band structure schematics for TCOs, wide band gap materials with sub-gap states near the CBM.

in Figure 6b. O-site substitution, on the other hand, results in a formation energy over 10 eV higher than that of an Sn site (not-shown), which suggests this defect-type is unlikely to occur.

We then consider the formation of Si_{Sn}-V_O defect clusters, where the Si atom takes one of the two symmetry inequivalent Sn sites neighboring the oxygen vacancy, marked by A and B on the right panel of Figure 6a. The calculated binding energies of the ionized Si_{Sn}-V_O clusters were found to be 0.757 eV on site A and 0.927 eV on site B. The positive binding energy suggests that Si substitutionals prefer to incorporate nearby undercoordinated Sn atoms.

As seen in Figure 7, in all cases, the electronic defect states associated with a V_O formation are not strongly affected by the presence of a neighboring Si atom. However, Figure 6b reveals that when the Si_{Sn}-V_O pair is formed, the thermodynamic transition energies $\epsilon(2/0)$ are shifted closer to the conduction band and values of Δ equal to 0.635 eV (site B) and 0.655 eV (site A) are obtained. The exponential dependence on the value of Δ suggests that a 25% shift observed in the presence of Si could significantly affect the ratio between the different charge states of oxygen vacancies present in the TCO. The presence of silicon is, accordingly, seen to promote the formation of ionized oxygen vacancies, that is, charge states that do not contribute to the parasitic absorption.

Finally, we validate our results by placing the Si_{Sn} and the V_O defects inside the same cell, but as far away from each other as the cell size allows, this defect geometry is shown in the left panel of Figure 6a. In the limit of an infinite cell, one should recover the exact sum of the behaviors of the two defects in isolation. Instead, Figure 6b reveals a small shift of 20 meV in the thermodynamic transition level $\epsilon(2/0)$, when compared to isolated V_O. Changes of similar magnitudes are seen in the electronic defect states, as shown in Figure 7. These shifts reflect the size of the error that results from the choice of the supercell and demonstrate the validity of the Si_{Sn}-V_O cluster calculations.

■ DISCUSSION

The increase in oxygen content in the Sn-based thin films when cosputtering with SiO_2 eliminates some V_O-related defects, subsequently improving the transparency of Sn-based TCOs. As the same optical/electrical trade-off cannot be achieved solely by tuning the oxygen partial pressure during deposition (Figure 1) or by mild annealing in air,[11] some additional effects linked to the presence of Si atoms are expected. Our DFT calculations show that the incorporation of Si atoms nearby oxygen-deficient sites is energetically favored, at least in the rutile SnO_2 lattice. This is due to a positive binding energy between a substitutional Si atom and a V_O. The binding of Si is further seen to promote the ionization of the oxygen defect, releasing charge carriers into the host material. Local structural relaxations following the ionization of V_O lead to electronic defect states at the edge of the optical band gap range and thus provide a potential explanation for the success of silicon in passivating optically detrimental states in Sn-based TCOs. A combination of the two phenomena, namely a direct passivation of V_O by the oxygen atoms of SiO_2 and an indirect passivation of V_O because of a shift of the electronic defect states to higher energies close to the band gap edge, could explain the experimental results shown in Figures 3 and 5. Interestingly, we report the same effect in both amorphous ZTO and mixed phase amorphous/polycrystalline SnO_2 samples, showing the generality of this "cold-passivation" approach.

■ CONCLUSIONS

In this work, we demonstrated an effective defect passivation scheme for Sn-based materials via SiO_2 addition. The addition of SiO_2 is experimentally seen to be equally effective for amorphous and mixed phase amorphous/polycrystalline microstructures. In addition, we provide a plausible explanation for the mechanisms governing the cold passivation using DFT calculations. The approach simultaneously preserves the electrical conductivity and improves the transparency of the films, opening new perspectives on low-temperature defect-selective passivation. The compatibility of this cosputtering methodology with temperature-sensitive processes and substrates (<200 °C) enables its application in transparent and flexible electronics. Finally, this approach should serve as an inspiration to design and discover oxides that could potentially play a similar role in other TCOs as SiO_2 does in SnO_2 and ZTO.

■ METHODS

Experimental Section. Thin films (150 nm) of SiZTO and $SiSnO_2$ were deposited onto aluminoborosilicate glass in a Leybold Univex RF sputtering system from separate targets of SnO_2, $Zn_{0.05}Sn_{0.3}O_{0.65}$, and SiO_2. Depositions were performed using two targets simultaneously, that is, ZTO and SiO_2 to deposit SiZTO or SnO_2 and SiO_2 to deposit $SiSnO_2$. The ZTO composition was optimized as described in ref 14. The power applied to the ZTO and SnO_2 targets was fixed to 80 W (1.02 W cm^{-2}), and the power on the SiO_2 target was varied

DOI: 10.1021/acs.jpcc.8b02302
J. Phys. Chem. C 2018, 122, 17612−17620

between 0, 15, and 20 W (up to 0.25 W cm^{-2}, all targets were 10 cm in diameter). Depositions with 5 W applied to the SiO_2 targets did not yield a stable plasma and were hence not performed. Before deposition, the pressure in the working chamber was ~6 × 10^{-7} mbar. Substrate temperatures of 100 and 25 °C were used for ZTO and SnO_2 respectively, because these conditions were found to yield high-quality films. Depositions were done with a constant flow of 10 sccm of Ar, whereas the O_2 partial pressure was changed by increasing or decreasing the flow of an Ar−O_2 gas mixture (95 at. % Ar and 5 at. % O_2) from 1.0 to 3.5 sccm to optimize the optoelectronic properties. The resulting working pressures were between 4 and 10 × 10^{-4} mbar. Following depositions, the films were subjected to a thermal treatment at 200 °C for 30 min in air using a hot plate. The free carrier densities and Hall mobilities of the films were obtained with a Hall effect HMS-5000 system in the Van der Pauw configuration. Their optical properties were measured using a PerkinElmer Lambda 900 spectrophotometer equipped with an integrating sphere. The absorptance of the films was calculated using the total transmittance and the total reflectance. To assess the microstructure and composition of the films, TEM was performed in FEI TITAN Themis (STEM EDX) or a FEI Osiris (nanobeam diffraction) microscope, both operated at 200 kV. Samples were characterized in cross section. Thin lamellae were extracted using the conventional focused-ion beam lift-out method in a Zeiss NVision 40. RBS spectrometry was used to assess the atomic concentration of the different atomic species in SiZTO and ZTO. During RBS measurements, high-energy He^{2+} ions are directed onto the samples, and the energy distribution and yield of the backscattered He^{2+} ions at a 160° angle is measured. For the calculation of the atomic concentration, the substrate and the background signals were subtracted. For the RBS measurements, uncertainties from statistical errors are shared for all films because all samples were deposited in the same sputtering system and were exposed to the same atmospheres and possible contaminants from the atmospheric environment. TDS was performed using an ESCO spectrometer equipped with a quadrupole mass spectrometer and a halogen lamp at a base pressure of 10^{-9} mbar. By comparing the total effusion and desorption rates from TDS, it was possible to compare total oxygen, tin and zinc desorption for ZTO and SiZTO while heating the samples at a constant rate of 20 °C/min up to 700 °C.

Defect Calculations. Thermodynamic transition levels $\epsilon(q_1/q_2)$ between two charged states q_1 and q_2 of a given defect show the Fermi energy, ϵ_F, at which the stable charge state changes. They were calculated using eq 2,

$$\varepsilon(q_1/q_2) = \frac{E_D^F(q_1, \varepsilon_F = \varepsilon_V) - E_D^F(q_2, \varepsilon_F = \varepsilon_V)}{q_2 - q_1} \quad (2)$$

where $E_D^F(q,\epsilon_F = \epsilon_V)$ is the formation energy of a defect D in a charge state q when the Fermi energy is set equal to the valence band maximum ϵ_V. Formation energies of the charged defects for each charge state were calculated using eq 3.

$$E_D^F = E_D{}^q - E_{SnO_2} - \sum_i n_i\mu_i + q\varepsilon_F + E_{cor} \quad (3)$$

where E_D^q is the energy of the supercell containing the defect D in a charge state q. E_{SnO_2} is the energy of the pure SnO_2 crystal in the same-sized supercell, n_i is the number of atoms of species i added to the supercell to create the defect, and μ_i is the chemical potential of that species. Chemical potential bounds were imposed by SnO_2 and SiO_2 formation. More detailed explanations of the methodology and the correction term, E_{cor}, applied to charged defect calculations can be found in ref 38.

The binding energy between two defects, X and Y, was calculated as the energy difference between the formation energies of the isolated defects and the formation energy of the X−Y defect cluster.

$$E^B = E_X^F + E_Y^F - E_{X-Y}^F \quad (4)$$

According to the definition in eq 4, a positive binding energy implies a preference for the two defects to cluster, whereas a negative binding energy suggests a preference for isolated defects. As the formation energy of a given defect (eq 3) depends on the Fermi level and the charge state of the defect, so does the binding energy.

Computational Details. All DFT calculations were performed using the PBE0 hybrid functional as implemented in the VASP electronic structure code.[41−44] Si 3s and 3p (4), O 2s and 2p (6), and Sn 5s, 5p, and 4d (14) electrons were included in the valence. All defects were introduced into a 2 × 2 × 3 (72 atom) supercell of rutile SnO_2 phase. The atomic positions were relaxed using a 2 × 2 × 2 Monkhorst−Pack k point mesh until the forces were below 0.02 eV/Å. Final densities of states were obtained using a 3 × 3 × 3 Γ-centered k-point mesh. The volume of the supercell was fixed to that of the (expanded) perfect crystal calculated via fitting the Birch−Murnaghan[45] equation of state. A 3 × 3 × 4 (216 atoms) supercell was tested to verify convergence with respect to supercell size, and a good qualitative agreement was found.

ASSOCIATED CONTENT

Supporting Information

The Supporting Information is available free of charge on the ACS Publications website at DOI: 10.1021/acs.jpcc.8b02302.

Deposition and optimization of $SiSnO_2$; thermal desorption spectroscopy; and XPS (PDF)

AUTHOR INFORMATION

Corresponding Authors

*E-mail: esteban.rucavado@epfl.ch (E.R.).
*E-mail: m.moralesmasis@utwente.nl (M.M.-M.).

ORCID

Miglė Graužinytė: 0000-0003-0369-8793
José A. Flores-Livas: 0000-0002-4183-1316
Takashi Koida: 0000-0001-8496-9166
Monica Morales-Masis: 0000-0003-0390-6839

Notes

The authors declare no competing financial interest.

ACKNOWLEDGMENTS

The authors thank Sylvain Dunand, Aymeric Schafflutzel, and Cedric Bucher for technical assistance with the sputtering system and Pierre Mettraux for XPS measurements. This work is funded by the SNSF Disco project (project number CRSII2_154474) and the SNSF international Short Visits program. J.A.F.-L. acknowledges computational resources under the project (s752), whereas M.G. and S.G. acknowledge the project s707 from the Swiss National Supercomputing

Center (CSCS) in Lugano. This research was partially supported by the NCCR MARVEL.

■ REFERENCES

(1) Song, S.-K.; Cho, J.-S.; Choi, W.-K.; Jung, H.-J.; Choi, D.; Lee, J.-Y.; Baik, H.-K.; Koh, S.-K. Structure and Gas-sensing Characteristics of Undoped Tin Oxide Thin Films Fabricated by Ion-assisted Deposition. *Sens. Actuators, B* **1998**, *46*, 42−49.

(2) Agashe, C.; Takwale, M. G.; Marathe, B. R.; Bhide, V. G. Structural properties of SnO2: F films deposited by spray pyrolysis. *Sol. Energy Mater.* **1988**, *17*, 99−117.

(3) Stjerna, B.; Olsson, E.; Granqvist, C. G. Optical and Electrical Properties of Radio Frequency Sputtered Tin Oxide Films Doped with Oxygen Vacancies, F, Sb, or Mo. *J. Appl. Phys.* **1994**, *76*, 3797−3817.

(4) Niedermeier, C. A.; Rhode, S.; Ide, K.; Hiramatsu, H.; Hosono, H.; Kamiya, T.; Moram, M. A. Electron Effective Mass and Mobility Limits in Degenerate Perovskite Stannate BaSnO3. *Phys. Rev. B* **2017**, *95*, 161202.

(5) Dixon, S. C.; Scanlon, D. O.; Carmalt, C. J.; Parkin, I. P. n-Type Doped Transparent Conducting Binary Oxides: an Overview. *J. Mater. Chem. C* **2016**, *4*, 6946−6961.

(6) Peng, H.; Bikowski, A.; Zakutayev, A.; Lany, S. Pathway to Oxide Photovoltaics via Band-structure Engineering of SnO. *APL Mater.* **2016**, *4*, 106103.

(7) Arai, T.; Iimura, S.; Kim, J.; Toda, Y.; Ueda, S.; Hosono, H. Chemical Design and Example of Transparent Bipolar Semiconductors. *J. Am. Chem. Soc.* **2017**, *139*, 17175−17180.

(8) Hennek, J. W.; Smith, J.; Yan, A.; Kim, M.-G.; Zhao, W.; Dravid, V. P.; Facchetti, A.; Marks, T. J. Oxygen "Getter" Effects on Microstructure and Carrier Transport in Low Temperature Combustion-Processed a-InXZnO (X = Ga, Sc, Y, La) Transistors. *J. Am. Chem. Soc.* **2013**, *135*, 10729−10741.

(9) Minami, T. Transparent and Conductive Multicomponent Oxide Films Prepared by Magnetron sputtering. *J. Vac. Sci. Technol. A* **1999**, *17*, 1765−1772.

(10) Frenzel, H.; Dörfler, T.; Schlupp, P.; von Wenckstern, H.; Grundmann, M. Long-throw Magnetron Sputtering of Amorphous Zn-Sn-O Thin Films at Room Temperature. *Phys. Status Solidi A* **2015**, *212*, 1482−1486.

(11) Rucavado, E.; Jeangros, Q.; Urban, D. F.; Holovský, J.; Remes, Z.; Duchamp, M.; Landucci, F.; Dunin-borkowski, R. E.; Körner, W.; Elsässer, C.; et al. Enhancing the Optoelectronic Properties of Amorphous Zinc Tin Oxide by Subgap Defect Passivation: A Theoretical and Experimental Demonstration. *Phys. Rev. B* **2017**, *95*, 245204.

(12) Dauzou, F.; Bouten, P. C. P.; Dabirian, A.; Leterrier, Y.; Ballif, C.; Morales-Masis, M. Mechanical Integrity of Hybrid Indium-free Electrodes for Flexible Devices. *Org. Electron.* **2016**, *35*, 136−141.

(13) Zhu, Q.; Ma, Q.; Buchholz, D. B.; Chang, R. P. H.; Bedzyk, M. J.; Mason, T. O. Structural and Physical Properties of Transparent Conducting, Amorphous Zn-doped SnO2 Films. *J. Appl. Phys.* **2014**, *115*, 033512.

(14) Morales-Masis, M.; Dauzou, F.; Jeangros, Q.; Dabirian, A.; Lifka, H.; Gierth, R.; Ruske, M.; Moet, D.; Hessler-Wyser, A.; Ballif, C. An Indium-Free Anode for Large-Area Flexible OLEDs: Defect-Free Transparent Conductive Zinc Tin Oxide. *Adv. Funct. Mater.* **2016**, *26*, 384−392.

(15) Chiang, H. Q.; Wager, J. F.; Hoffman, R. L.; Jeong, J.; Keszler, D. A. High Mobility Transparent Thin-film Transistors with Amorphous Zinc Tin Oxide Channel Layer. *Appl. Phys. Lett.* **2005**, *86*, 013503.

(16) Han, S.; Lee, S. Y. Full Swing Depletion-load Inverter with Amorphous SiZnSnO Thin Film Transistors. *Phys. Status Solidi A* **2017**, *214*, 1600469.

(17) Werner, J.; Walter, A.; Rucavado, E.; Moon, S.-J.; Sacchetto, D.; Rienaecker, M.; Peibst, R.; Brendel, R.; Niquille, X.; De Wolf, S.; et al. Zinc Tin Oxide as High-temperature Stable Recombination Layer for Mesoscopic Perovskite/Silicon Monolithic Tandem Solar Cells. *Appl. Phys. Lett.* **2016**, *109*, 233902.

(18) Körner, W.; Elsässer, C. Density-functional theory study of stability and subgap states of crystalline and amorphous Zn-Sn-O. *Thin Solid Films* **2014**, *555*, 81−86.

(19) Körner, W.; Gumbsch, P.; Elsässer, C. Analysis of Electronic Subgap States in Amorphous Semiconductor Oxides Based on the Example of Zn-Sn-O Systems. *Phys. Rev. B: Condens. Matter Mater. Phys.* **2012**, *86*, 165210.

(20) Wolf, S. D.; Descoeudres, A.; Holman, Z. C.; Ballif, C. High-efficiency Silicon Heterojunction Solar Cells: A Review. *Green* **2012**, 7−24.

(21) Morales-Masis, M.; De Wolf, S.; Woods-Robinson, R.; Ager, J. W.; Ballif, C. Transparent Electrodes for Efficient Optoelectronics. *Adv. Electron. Mater.* **2017**, *3*, 1600529.

(22) Werner, J.; Niesen, B.; Ballif, C. Perovskite/Silicon Tandem Solar Cells: Marriage of Convenience or True Love Story? - An Overview. *Adv. Mater. Interfaces* **2017**, *5*, 1700731.

(23) Dabirian, A.; Martin de Nicolas, S.; Niesen, B.; Hessler-Wyser, A.; De Wolf, S.; Morales-Masis, M.; Ballif, C. Tuning the Optoelectronic Properties of ZnO:Al by Addition of Silica for Light Trapping in High-Efficiency Crystalline Si Solar Cells. *Adv. Mater. Interfaces* **2016**, *3*, 1500462.

(24) Kizu, T.; Aikawa, S.; Nabatame, T.; Fujiwara, A.; Ito, K.; Takahashi, M.; Tsukagoshi, K. Homogeneous Double-layer Amorphous Si-doped Indium Oxide Thin-film Transistors for Control of Turn-on Voltage. *J. Appl. Phys.* **2016**, *120*, 045702.

(25) Mitoma, N.; Aikawa, S.; Gao, X.; Kizu, T.; Shimizu, M.; Lin, M.-F.; Nabatame, T.; Tsukagoshi, K. Stable amorphous In2O3-based thin-film transistors by incorporating SiO2 to suppress oxygen vacancies. *Appl. Phys. Lett.* **2014**, *104*, 102103.

(26) Kang, I. J.; Park, C. H.; Chong, E.; Lee, S. Y. Role of Si as carrier suppressor in amorphous Zn-Sn-O. *Curr. Appl. Phys.* **2012**, *12*, S12−S16.

(27) Minami, T.; Sato, H.; Nanto, H.; Takata, S. Highty Conductive and Transparent Silicon Doped Zinc Oxide Thin Films Prepared by RF Magnetron Sputtering. *Jpn. J. Appl. Phys.* **1986**, *25*, L776−L779.

(28) Faure, C.; Clatot, J.; Teulé-Gay, L.; Campet, G.; Labrugère, C.; Nistor, M.; Rougier, A. Co-sputtered ZnO:Si thin films as transparent conductive oxides. *Thin Solid Films* **2012**, *524*, 151−156.

(29) Rashidi, N.; Kuznetsov, V. L.; Dilworth, J. R.; Pepper, M.; Dobson, P. J.; Edwards, P. P. Highly Conducting and Optically Transparent Si-doped ZnO Thin Films Prepared by Spray Pyrolysis. *J. Mater. Chem. C* **2013**, *1*, 6960.

(30) Clatot, J.; Campet, G.; Zeinert, A.; Labrugère, C.; Nistor, M.; Rougier, A. Low Temperature Si Doped ZnO Thin Films for Transparent Conducting Oxides. *Sol. Energy Mater. Sol. Cells* **2011**, *95*, 2357−2362.

(31) Sorar, I.; Saygin-Hinczewski, D.; Hinczewski, M.; Tepehan, F. Z. Optical and Structural Properties of Si-doped ZnO Thin Films. *Appl. Surf. Sci.* **2011**, *257*, 7343−7349.

(32) Choi, J. Y.; Heo, K.; Cho, K.-s.; Hwang, S. W.; Kim, S.; Lee, S. Y. Engineering of Band Gap States of Amorphous SiZnSnO Semiconductor as a Function of Si Doping Concentration. *Sci. Rep.* **2016**, *6*, 36504.

(33) Shard, A. G. Detection limits in XPS for more than 6000 binary systems using Al and Mg Kα X-rays. *Surf. Interface Anal.* **2014**, *46*, 175−185.

(34) Watts, J.; Wolstenholme, J. *Introduction to Surface Analysis by XPS and AES*; Wiley, 2003.

(35) Summitt, R.; Marley, J. A.; Borrelli, N. F. The ultraviolet absorption edge of stannic oxide (SnO2). *J. Phys. Chem. Solids* **1964**, *25*, 1465−1469.

(36) Kılıç, Ç.; Zunger, A. Origins of Coexistence of Conductivity and Transparency in SnO2. *Phys. Rev. Lett.* **2002**, *88*, 095501.

(37) Guo, D.; Hu, C. First-principles Study on the Electronic Structure and Optical Properties for SnO2 with Oxygen Vacancy. *Appl. Surf. Sci.* **2012**, *258*, 6987−6992.

DOI: 10.1021/acs.jpcc.8b02302
J. Phys. Chem. C 2018, 122, 17612−17620

(38) Graužinytė, M.; Goedecker, S.; Flores-Livas, J. A. Computational Screening of Useful Hole−Electron Dopants in SnO2. *Chem. Mater.* **2017**, *29*, 10095−10103.
(39) Lany, S.; Zunger, A. Dopability, Intrinsic Conductivity, and Nonstoichiometry of Transparent Conducting Oxides. *Phys. Rev. Lett.* **2007**, *98*, 045501.
(40) Lany, S.; Zunger, A. Anion Vacancies as a Source of Persistent Photoconductivity in II-VI and Chalcopyrite Semiconductors. *Phys. Rev. B: Condens. Matter Mater. Phys.* **2005**, *72*, 035215.
(41) Kresse, G.; Furthmüller, J. Efficient iterative schemes forab initiototal-energy calculations using a plane-wave basis set. *Phys. Rev. B: Condens. Matter Mater. Phys.* **1996**, *54*, 11169−11186.
(42) Kresse, G.; Furthmüller, J. Efficiency of ab-initio total energy calculations for metals and semiconductors using a plane-wave basis set. *Comput. Mater. Sci.* **1996**, *6*, 15−50.
(43) Paier, J.; Marsman, M.; Hummer, K.; Kresse, G.; Gerber, I. C.; Ángyán, J. G. Screened Hybrid Density Functionals Applied to Solids. *J. Chem. Phys.* **2006**, *124*, 154709.
(44) Adamo, C.; Barone, V. Toward Reliable Density Functional Methods without Adjustable Parameters: The PBE0 Model. *J. Chem. Phys.* **1999**, *110*, 6158−6170.
(45) Birch, F. Finite Elastic Strain of Cubic Crystals. *Phys. Rev.* **1947**, *71*, 809−824.

DOI: 10.1021/acs.jpcc.8b02302
J. Phys. Chem. C 2018, 122, 17612−17620